

# Quantitative diffusion-weighted MRI analysis algorithms

Judit Ben Ami<sup>1</sup>, Marina Khizgilov<sup>1</sup>, Moti Freiman<sup>1</sup>

<sup>1</sup> Department of Biomedical Engineering, Technion - IIT, Haifa, Israel

**Abstract:** Tissue characterizations are strongly dependent on its health condition. Various diseases such as different types of cancer or inflammatory activities (e.g. Crohn's disease) may change tissue structure, thus changing its diffusivity. Intravoxel incoherent motion (IVIM) imaging is a non-invasive MRI technique sensitive to tissue diffusivity characteristics. It is modeled by 3 IVIM parameters: diffusion coefficient (D), which reflects the motion of molecules inside the tissue; pseudo-diffusion coefficient (D\*), which reflects microcapillary perfusion; and perfusion fraction (f), which reflects the relative area of capillaries. The main objective of this project is to implement a post-processing tool for IVIM parameters quantifications, thus providing a new, non-invasive, radiation-free diagnostics method in various clinical applications, such as diagnosis of diseases and prediction of treatment response.

For the objective stated above, a multi-purpose Python library was created which includes four IVIM parameters estimation algorithms: Segmented Doubly Linearized Least Squares (SEGb), Segmented Partially Linearized Least Squares (SEG), Full Nonlinear Least Squares (LSQ), and Bayesian modeling with a Gaussian shrinkage prior (BSP). The results were compared by calculating the relative errors. LSQ and BSP methods consistently outperformed the SEG and SEGb methods, providing lower relative errors, as well as visually pleasing IVIM parameters maps with reduced erroneous heterogeneity. However, satisfactory results of the BSP method were not achieved and the full potential of the algorithm was not reached.

**Keywords:** Diffusion-Weighted MRI, Model fitting algorithms, post-processing, IVIM parameters, b-value, Python

## 1. Introduction

Diffusion-weighted MRI (DW-MRI) is a non-invasive MRI technique sensitive to the motion of molecules inside the body.

In the past, the use of this technique was confined largely to the brain, evaluating intracranial diseases. Today, due to numerous technological advances, it is possible to translate this technique to other body sites, such as abdomen, breast, and pelvis. Such translation provides information about the tissue structure, which previously was unknown or was extracted using invasive clinical applications such as biopsy or colonoscopy.

Using this technique, several DW-MRI images are acquired, each at different b-value [s/mm<sup>2</sup>], a parameter that represents the time the particles in the tissue had to perform diffusion, and the magnitude of the envelope. Molecules with a larger degree of motion or greater diffusion distance will show signal attenuation with small b-values, whereas slow-moving molecules will require higher b-values to show apparent signal attenuation.

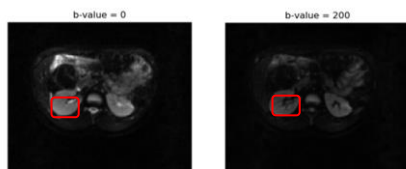


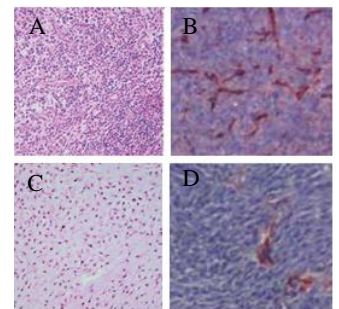
**Fig. 1: DW-MRI images of the kidneys taken at two different b-values [s/mm<sup>2</sup>].** Signal remains only in a restricted diffusion region. Images from Boston Children's hospital Database.

The attenuation of the signal is assumed to be caused by two biomarkers: slow diffusion, which is associated with cell density, and fast diffusion, which is associated with tissue microcirculation. By observing the attenuation of the signal, it is possible to characterize tissue structure and distinguish between different parts of it, showing great potential at various clinical applications, such as characterization of inflammatory activity in the body (e.g. Crohn's disease), prediction of treatment response, and detection and separation between benign and malignant tumours.

A simplified model describing the relationship between signal attenuation and increasing b-values is given by the formula:

$$(1) s_i = s_0 e^{-b_i \cdot ADC}$$

Where  $s_i$  is the signal obtained with the  $i^{\text{th}}$  b-value,  $b_i$ ,  $s_0$  is the signal with  $b=0$ , and  $ADC$  [mm<sup>2</sup>/s] is the apparent diffusion coefficient, a quantitative measure of tissue diffusivity [2]. However, clinical applications of this model have shown that it is not capable of differentiating between different types of diffusion. For example, for tumorous tissue with high cellular density and high microcirculation, the expected slow diffusion



Ginat et al. 2012 Edrei et al. 2012

**Fig. 2 [11, 12]: Microscopic images of tissue.** (A) High cell density, slow-diffusion (B) High microcirculation, fast diffusion (C) Low cell density, slow-diffusion (D) Low microcirculation, fast diffusion.

will be low, making the DW-MRI image brighter on the one hand, but the expected fast diffusion will be high, making the DW-MRI image darker on the other: In that case, ADC model is not able to differentiate between different types of diffusions, averaging the result instead. Encapsulation of contradicting phenomenon accrues, and an abnormal tissue structure may seem healthy.

An additional model to describe relative signal attenuation as a function of b-values, was suggested by Le Beihan et al. [8] in 1986. This model is based on the principles of intravoxel incoherent motion (IVIM) and states the function that describes the DW-MRI data is of biexponential matter and is given by the formula:

$$(2) s_i = s_0 (f \cdot e^{-b_i(D^*+D)} + (1-f) \cdot e^{-b_i D})$$

Where  $f$  [a.u.] is the perfusion fraction,  $D^*$  [ $\text{mm}^2/\text{s}$ ] and  $D$  [ $\text{mm}^2/\text{s}$ ] represent the pseudo-diffusion and diffusion coefficients, respectively. Together,  $D$ ,  $D^*$  and  $f$  are called the IVIM parameters.

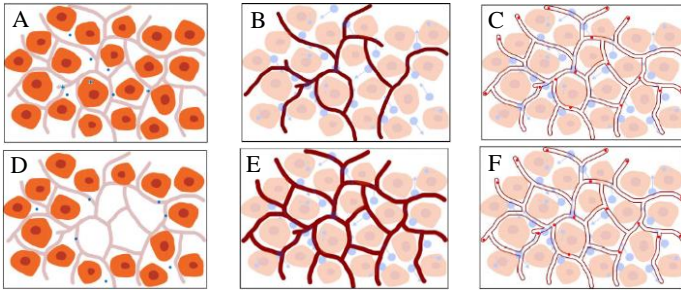


**Fig. 3: Intra-Voxel Incoherent Motion model parameters illustration.** (A) Restricted diffusion, low  $D$  (B) Decreased capillaries' volume, low  $f$  (C) Decreased blood flow, low  $D^*$  (D) Unrestricted diffusion, high  $D$  (E) Increased capillaries' volume, high  $f$  (F) Increased blood flow, high  $D^*$ .

usually, pseudo-diffusion parameter,  $D^*$ , has much higher values than diffusion parameter,  $D$ , which means that for any given b-value, the pseudo-diffusion term decays faster than the diffusion term. With high b-values ( $b > 200 \text{ s/mm}^2$  [2]), diffusion plays a dominant role while the contribution of perfusion is minimal, meaning that for accurate estimation of IVIM parameters, DW-MRI images must be acquired with both high and low b-values.

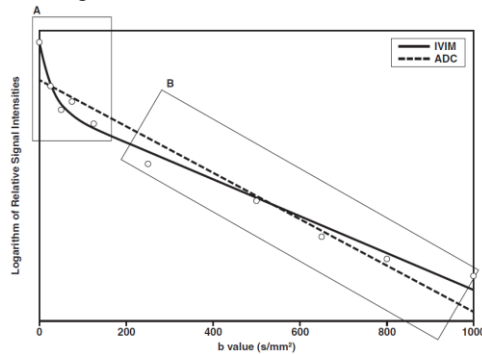


**Fig. 4 [2] : Plot of logarithm of relative signal intensity as a function of b-value, taken from normal liver parenchyma of a 30-year-old man (solid line).** For IVIM model, steeper decrease

for lower b-values (A) is observed while for higher b-values (B) the attenuation is more gradual. In addition, plot of the ADC model is present (dotted line).

After data acquisition, proper fitting methods are acquired for quantification accuracy of IVIM parameters, as quality of the fit is strongly influenced by the signal-to-noise (SNR) ratio of the DW-MRI images.

As this project's aim was to build a post-processing tool for IVIM parameters estimation, a Python library consisting of estimation algorithms was built. In this study, the different IVIM parameters estimations algorithms are presented, along side with comparison between them.

## 2. Methods

The project presented in this paper aims to implement a complete and general solution for DW-MRI images post processing, based on the bi-exponential model presented in eq 2. The post processing tool input is a set of DW images taken at different b-values, and the tool's output is three IVIM parameters maps:  $D$  map,  $D^*$  map and  $f$  map, each emphasizes a different quality of the tissue as describes in the introduction.

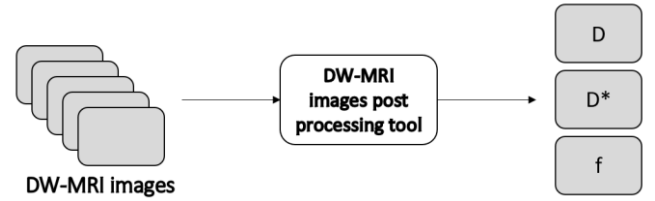


**Fig. 5: DW-MRI images post processing tool inputs and outputs.** The tool gets a set of DW-MRI images, all in the same size and at different b-values. Using the input images the tool estimates and outputs the three IVIM parameters maps, each map is the size of the original images and represents the value of the relevant IVIM parameter in each voxel.

The IVIM parameters estimation is done by four different algorithms: the first three use least squares approach stating that every voxel is estimated independently to its neighboring voxels, and the last algorithm use Bayesian approach stating that every voxel is estimated with consideration to its neighboring voxels.

For mathematical convenient, all the analysis is done with the normalized signal,  $y_i$  ( $0 \leq y_i \leq 1$ ):

$$(3) y_i \triangleq \frac{s_i}{s_0} = f e^{-b_i(D^*+D)} + (1-f) e^{-b_i D}$$

### 2.1. Segmented Doubly Linearized Least Squares (SEGb)

The first and the simplest method for IVIM parameters estimation is SEGb. In this approach the estimation is done separately for low b-values and high b-values: for high b-values it is assumed that the pseudo-diffusion component has entirely decayed away [3], thus the model from eq.3 is given proximally by:

$$(4) y_i = (1-f) e^{-b_i D}$$

By taking the natural logarithm of both sides of eq.4, a linearized least squares fit can be applied in order to obtain an estimation of  $D$  from slope and  $f$  from intercept:

$$(5) \ln(y_i) = \ln(1-f) - b_i D$$

With D and f fixed, the final parameter D\* is estimated by a second linearized least squares fit for low b-values where it assumed that the pseudo-diffusion component is more significant than the diffusion component. Applying this assumption to eq.3 results in the formula:

$$(6) \quad y_i = fe^{-b_i(D^*+D)}$$

By taking the natural logarithm of both sides of eq.6, a linearized least squares fit can be applied in order to obtain an estimation of D\* from slope:

$$(7) \quad \ln(y_i) = \ln(f) - b_i(D^*+D)$$

For all IVIM parameters physiological constrains have been set according to eq.8 [6], and if a value exceeds those bounds the parameter is set to be the closest limit.

$$(8) \quad \begin{aligned} 0 \leq D \leq 0.02 \text{ mm}^2 / s \\ 0 \leq D^* \leq 1.1 \text{ mm}^2 / s \\ 0 \leq f \leq 1 \end{aligned}$$

The main advantage of this method is that no starting guesses are required. In addition, its low complexity allows a simple algorithm implementation and a low runtime. However, it is the least accurate from all the four methods mentioned.

## 2.2. Segmented Partially Linearized Least Squares (SEG)

In this method for IVIM parameters estimation D and f are estimated the same way as in SEGb method: by linearized least squares for high b-values as described in eq.5. With D and f fixed, the final parameter D\* is estimated by performing a non-linear constrained least squares fit to eq.3. The constrains (eq.8) are required due to physiological limitations and are the same in all methods. Note that nonlinear least squares requires a starting guess for D\*. In this project the starting guess was taken to be the value of D\* estimated by SEGb method.

SEG has higher complexity than SEGb but lower complexity than LSQ and BSP. In addition, SEG is slower than SEGb but significantly faster than LSQ and BSP, and is more accurate than SEGb for D\* estimation.

## 2.3. Segmented Partially Linearized Least Squares (LSQ)

In this method no separation to low and high b-values is needed. The IVIM parameters are estimated all together, simultaneously, on a voxel-by-voxel basis by nonlinear constrained least squares fit to eq.3. The starting guess chosen in this work is the IVIM parameters estimated using SEG, and the constrains are chosen according to eq.8.

This method has higher complexity than SEGb and SEG but lower than BSP, and accordingly it is slower than SEGb and SEG but faster than BSP. It is more accurate than SEGb and SEG.

## 2.4. Bayesian Shrinkage Prior (BSP)

The last and most complex algorithm used in this work is BSP. The basic idea of BSP is to iteratively maximize a joint posterior probability of IVIM parameters for an M-size environment, given the observed data:

$$(9) \quad p(\theta_{1:M}, \mu, \Sigma_\mu | y_j) \propto \prod_{j=1}^M p(y_j | \theta_j) p(\theta_j | \mu, \Sigma_\mu)$$

Where  $\theta_j = (d_j, d_j^*, F_j)$  is a vector of three IVIM parameters in the following transformed form:

$$(10) \quad \begin{aligned} d &= \log(D) \\ d^* &= \log(D^*) \\ F &= \log(f) - \log(1-f) \end{aligned}$$

and  $\mu, \Sigma_\mu$  are the mean vector and the covariance matrix of the transformed parameter, accordingly, over all M voxels. The prior function  $p(\theta_j | \mu, \Sigma_\mu)$  subjects to a 3xM multivariate Gaussian distribution [4]. The likelihood function is an N-dimension multivariate conditional probability, where N is the number of b-values, that takes the form [6]:

$$(11) \quad p(y_j | \theta_j) \propto [y^T y - (y^T g)^2 / (g^T g)]^{-N/2}$$

Where y is the normalized original signal value (the input) as mentioned before, and g is the reconstructed image generated according to eq.3 based on estimated IVIM parameters.

The iteration process for fitting is done by Markov chain Monte Carlo (MCMC) algorithm [4], as illustrated in fig.6. BSP method also requires starting guess – the IVIM parameters estimated using LSQ method.

From all the methods mentioned, BSP is the only method that takes into consideration the voxel environment and thus the most robust to noise. However, it has the highest complexity from all.

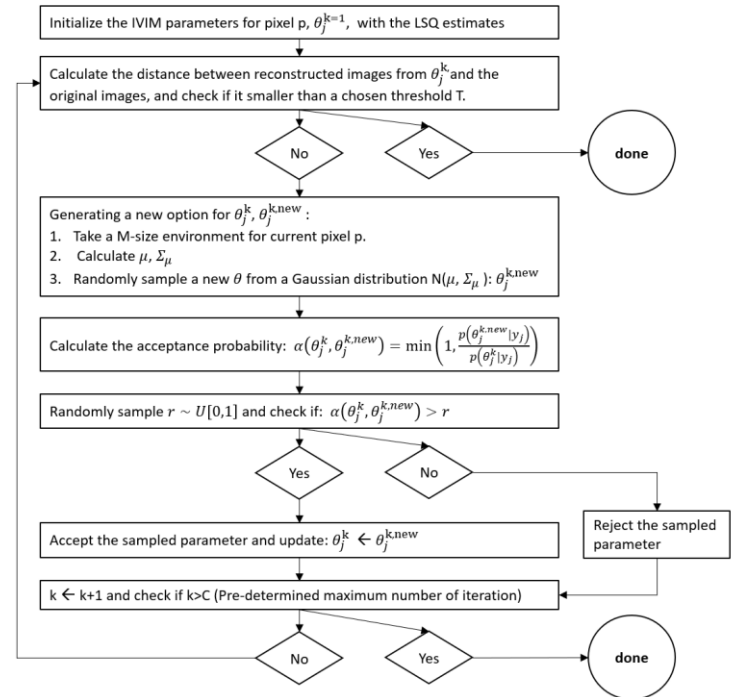


**Fig. 6: Flow chart of BSP inference.** The algorithm is done per voxel, iteratively. k - number of iterations, j - voxel number. Parameters of the method: M - size of a square environment around the voxel j, T - threshold for decision for convention, C - maximum number of iterations.

### 3. Results and Discussion

#### 3.1. Library Implementation

The solution provided is a free and accessible Python library that includes the following functions: (1) images to ndarray function; (2) generating simulation images function; (3) IVIM parameters maps estimation function; (4) error analysis function for comparing two sets of IVIM maps (e.g. known from simulation versus estimated); (5) error analysis function for comparing two sets of DW-MRI images (e.g. original images versus images that were reconstructed by the estimated IVIM parameters maps).

The usage in the library is divided into two main branches as described in fig.7: it works either on phantom images or on clinical DW-MRI images.

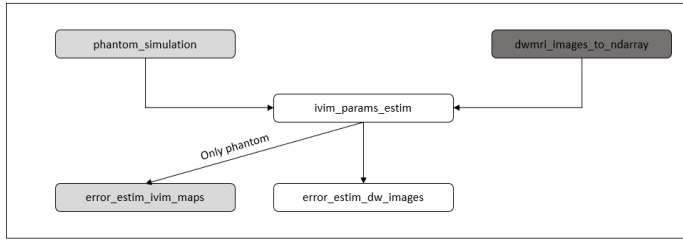


**Fig. 7: Python library functions.** The above chart shows the 5 functions the library contains and the 2 main ways to use it: one way is working solely on simulation; the first step is to create simulated DW images ('phantom\_simulation' function). The simulated DW images are used as input for the main function that estimates the IVIM parameters maps ('ivim\_params\_estim'). Finally, the user can assess the error in one of two ways: compare the output IVIM parameters maps to the known maps that were generated by the simulation ('error\_estim\_ivim\_maps'), or to reconstruct the DW images from the estimated parameters and compare them to the original DW images that were generated by the simulation ('error\_estim\_dw\_images'). The second mode of working with the library is with clinical DW-MRI images: first, the user should convert the images to ndarray form('dwmri\_images\_to\_ndarray'). The converted DW-MRI images are used as an input for IVIM parameters estimation function. Finally, an error evaluation can be made based on the reconstructed images.

A full documentation and the complete library are available at the link below:

<https://github.com/tcml-judit-marina/IvimParamsEstimLib>

##### 3.1.1. Function: 'ivim\_params\_estim'

The function 'ivim\_params\_estim' is the main function of the library and its inputs and outputs are described in fig.5.

The function contains all four methods of IVIM parameters estimation. Note that the chosen method is an input to the function, as well. Due to the need and importance of the starting guess, the methods are implemented one by one, ordered by their complexity, as illustrated in fig. 8.

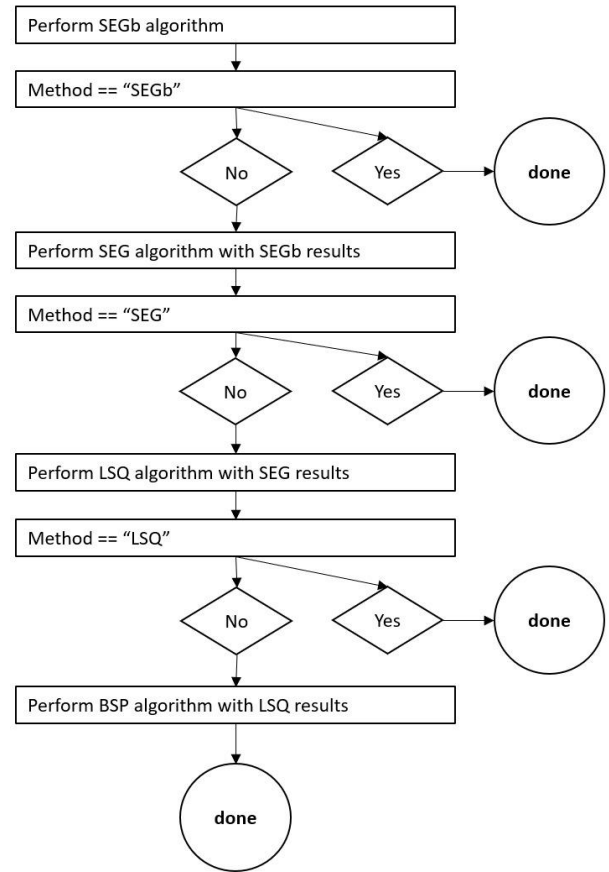


**Fig. 8: 'ivim\_params\_estim' function implementation flow chart.**

##### 3.1.2. Special Features

Other than functionality, an inseparable part of the library is its special features and speed. For control and debug, an optional debug flag was implemented, which allows printing the code progress in order to monitor runtime and BSP conversion.

To avoid runtime errors, input checks are done for all functions. Extended use of exceptions and assertions is presented.

Finally, for speed and efficiency, vectorize programming is being used and multiprocessing is implemented for SEG and LSQ (fig.9). Multiprocessing results depends on the hardware available, on the SNR of the images and the size of the images. The bigger and noisier the image, the longer it will take for the code to run. Using multiprocessing improves runtime significantly in a non-linear manner, and for large and complex images the relative improvement is even better.

	SEG runtime [minutes]		LSQ [minutes]	
	with multiprocessing	without multiprocessing	with multiprocessing	without multiprocessing
simulation images images dimensions: 64x64 (fig.10)	0.3	0.4	0.33	0.24
clinical DW-MRI images images dimensions: 156x162 (fig.14)	0.63	0.83	4.49	8.65

**Fig. 9: Multiprocessing versus non-multiprocessing results for SEG and LSQ implementations.** The results are for the analyzed examples from sections 3.2. and 3.3.



### 3.2. Phantom Simulation Results

As mentioned before – one of the modes to use the library is via simulation. In this subsection an example is presented. First, artificial phantom images have been created: the phantom is in the form of  $P$  concentric circles, where  $P$  can be chosen by the user. In the current example  $N$  chosen to be 3 (with background the total number of regions in the phantom is 4). The images were set to be in the size of 64x64 pixels, and 8 different  $b$ -values were chosen: [0, 20, 40, 100, 250, 350, 500, 800] [s/mm<sup>2</sup>]. In addition, a Gaussian noise with SNR of 0.001 was added in order to simulate clinical DW-MRI images.

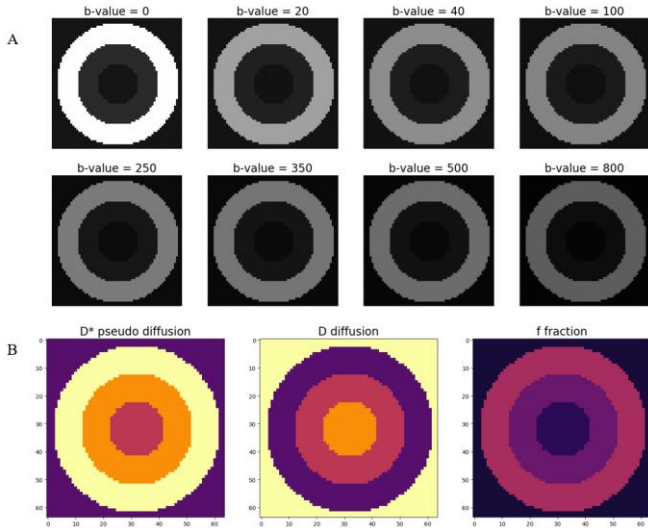


**Fig. 10: Phantom simulation.** (A) Simulated DW images created by phantom creating function, noise added (Gaussian noise with SNR of 0.001). (B) IVIM parameters maps created by phantom creating function. The DW images in (A) were generated from the IVIM parameters maps in (B) according to eq. 2.

Afterwards, the simulated DW images were analyzed by the IVIM parameters estimation function, and IVIM maps were extracted. All the methods were implemented, and the resulted IVIM maps parameters for each method (SEGb, SEG, LSQ, BSP) are shown in fig.11. Visually one can see clearly an improvement from SEGb to SEG, and from SEG to LSQ. However, contrary to expectations, no apparent improvement from LSQ to BSP was observed. In addition, it is very noticeable that the estimation for  $D^*$  parameter is the most challenging, and SEGb for example almost can't assess it.

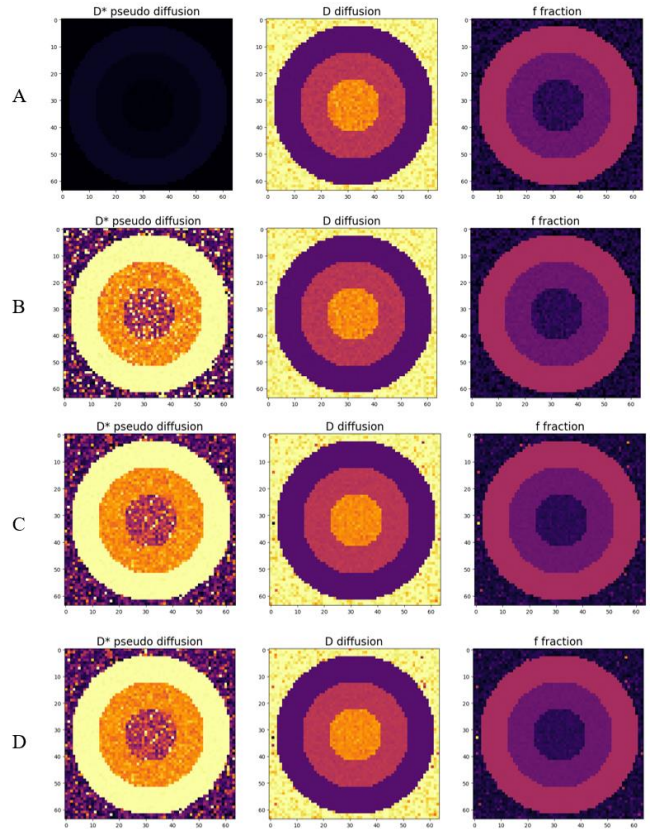


**Fig. 11: Estimated IVIM parameters maps of simulated phantom.** Maps were estimated using following algorithms: (A) SEGb (B) SEG (C) LSQ (D) BSP.

Quantitative error analysis has also been performed in two different ways: the first one is by comparing the IVIM parameters maps directly (known versus estimated), and the second is by comparing the original images to the reconstructed images from the estimated IVIM maps. The quantitative error analysis is shown in fig. 12, and they support the visual appearance from fig.10 as mentioned before: LSQ and BSP has the lowest error, SEG is less accurate and the least accurate method is SEGb. BSP and LSQ performance was similar and no improvement has accrued from as a result of using BSP and not just LSQ. Of course, this result is surprising because the Bayesian character of BSP and the consideration in neighboring voxels should have outcome with much better results, also as supported in literature [3, 4, 5, 6, 7].

	SEGb	SEG	LSQ	BSP
<b>D map</b>	3.09%	3.09%	2.45%	2.49%
<b>D* map</b>	94.96%	70.95%	29.41%	29.53%
<b>f map</b>	13.69%	13.69%	12.04%	11.98%
<b>mean IVIM maps</b>	37.25%	29.24%	14.64%	14.67%
<b>DW images</b>	16.74%	0.79%	0.73%	0.74%

**Fig 12: Quantitative error analysis for phantom simulation results (fig. 11).** The errors are relative errors in percentage, and each cooperation has been done for all 4 methods.

Finally, the relationship between b-value and the estimation accuracy has been observed in fig. 13: it is clearly shown that SEGb has the worst fit to the original data, as expected. However, for the observed pixel, SEG, LSQ and BSP has very similar results. In addition, one can see that the higher the b-value is than the error decreases, as expected [2].

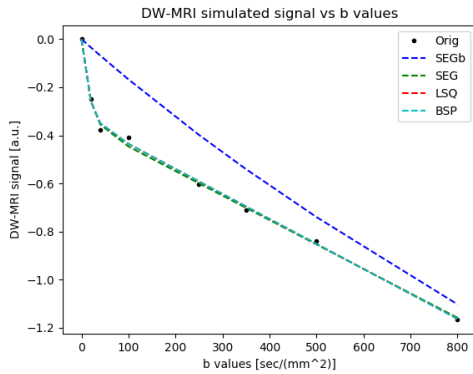


**Fig. 13: Plot of logarithm of normalized signal intensity as a function of b-value for a single voxel, from phantom simulation.**

### 3.3. Clinical Results

DW-MRI images of abdomen area from Boston Children's hospital database were analysed using implemented IVIM parameters quantification algorithms: SEGb, SEG, LSQ, BSP.

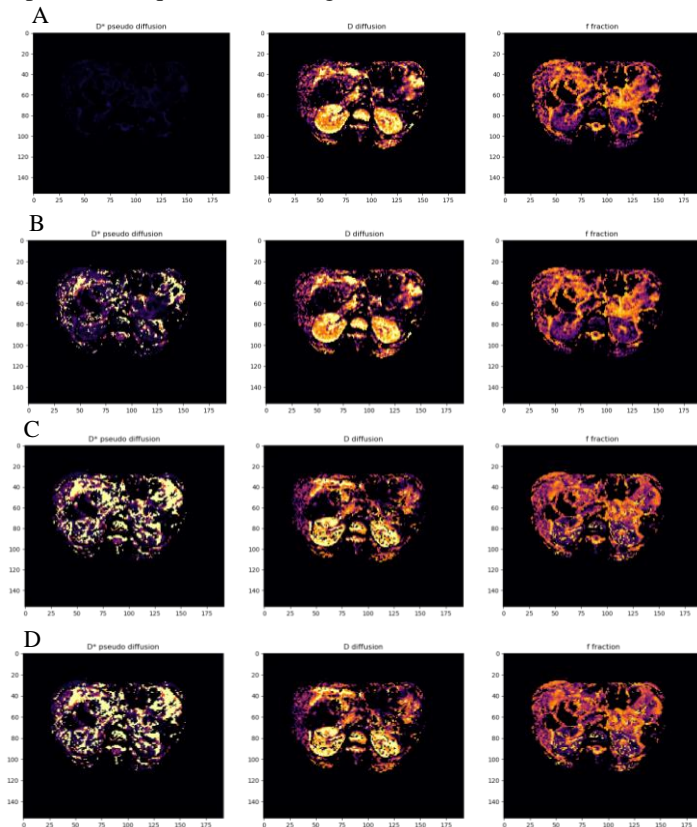


**Fig. 14 : Estimated IVIM parameters maps of healthy individual, showing transverse plane of kidneys. Maps were estimated using following algorithms: (A) SEGb (B) SEG (C) LSQ (D) BSP.**

LSQ and BSP algorithms have better visual results than SEGb and SEG methods, as expected. For error calculation, voxels with signal value lower than 50 [6] were set to zero, as such voxels belong to the DW-MRI images background and not to physiological tissue. Then, relative error between original images and reconstructed images using IVIM parameters maps were estimated. For SEGb and SEG the relative errors were 6.8% and 3.2%, respectively. The relative errors for LSQ and BSP were approximately the same: 2.53% for LSQ and 2.55% for BSP. Those results did not match with previous clinical IVIM parameters estimation results in literature [6,3]. This mismatch between the project's results and literature expectations is both in clinical images and simulated images (fig.11). In order to address this matter, a simple test has been implemented: A small square of pixels (size 5x5) of the same grey level was created. Noise was added. IVIM parameters estimation algorithms were applied. The BSP algorithm results were as expected and indeed outperformed the LSQ results, meaning that the mismatch apparently occurs due to the transformation from small and simple images to larger and more complicated images. Any one of BSP parameters mentioned in fig.6 (M, T, C) can be the cause.

In addition, note that D\* map have worse visual characteristics than D and f maps. This can be explained by several facts: firstly, D\* term is non-linear, thus it is harder to quantify it. Also, for any given b-value, D\* term decay is faster than D term decay, therefore the number of meaningful samples of D\* is lower than any other term, making D\* parameter estimation less accurate than D and f parameters. Lastly, due to MRI's physical properties, lower b-values are more prone to measurement errors and are highly sensitive to SNR variations, thus posing significant challenges to model fitting. [9,10]

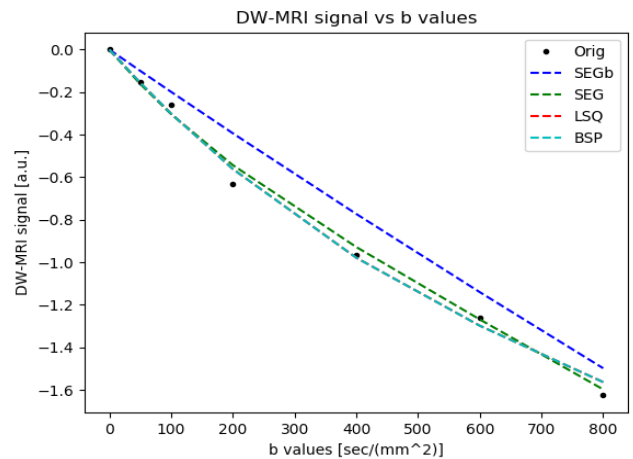


**Fig. 15: Plot of logarithm of relative signal intensity as a function of b-value for a single voxel, from DW-MRI image, using four estimation algorithms. In dots, original signal is given. LSQ and BSP show a better fit than SEGb and SEG to the original signal.**

## 4. Conclusions

DW-MRI is a non-invasive, radiation free imaging technique that can provide a new insight on tissue structure, making it a powerful tool for clinical applications in various body sites. However, DW-MRI data acquisition by itself is not enough to get the desirable information about tissue characteristics. By applying IVIM model to describe the relative signal attenuation as a function of b-value, IVIM parameters, parameters of the model that carry the information regarding different types of diffusion in body, can be quantified.

For this purpose, a multi purpose Python library was created. This library includes: four model fitting algorithms for IVIM parameters estimation, phantom creating function, images to ndarray converting function, and error calculation functions. In addition, for robustness, efficiency and higher performance, the library uses vectorize programming, multiprocessing, assertions and exceptions.

While BSP and LSQ methods outperformed SEG and SEGb as expected, producing more visually pleasing IVIM maps and lower relative error between original images and reconstructed images from estimated IVIM maps (2.55% for BSP, 2.53% for SEG), BSP, in contrary to expectations, did not give better results than LSQ [6,3]. This might be due to inaccurate choice of BSP parameters such as environment size, maximum number of possible iteration or convergence criteria.

In conclusion, quantification of fast and slow diffusion from DW MRI data is challenging due to the low SNR and the large number of variables compared to the number of observations, but is possible using the approaches mentioned above. Future work should be directed to improve current BSP implementation. In addition, more Bayesian approach methods (Fusion Bootstrap Moves (FBM) and FBM with segmented updating (FBMb) [3]) should be implemented in order to increase the tool's functionality. Also, new approaches should be considered, such as machine learning and convolutional neural network (CNN).

## Acknowledgements

The project was supported by the Department of Biomedical Engineering, Technion - IIT, Haifa, Israel.

The authors would like to thank Dr. Anat Grinfeld from the Department of Medical Imaging, Rambam Health Care Campus, Haifa, Israel, for her meaningful insights and support throughout the project.

The authors would also like to thank MSc candidate Elad Rotman for taking part in the implementation of phantom creating function.

## References

[1] Koh DM, Collins DJ. Diffusion-Weighted MRI in the body: applications and challenges in oncology. *AJR* 188:1622-1635, (2007).

[2] Koh DM, Collins DJ, Orton MR. Intravoxel incoherent motion in body diffusion-weighted MRI: reality and challenges. *AJR* 196:1351-1361, (2011).

[3] While PT. A comparative simulation study of Bayesian fitting approaches to intravoxel incoherent motion modeling in diffusion-weighted MRI. *Magnetic Resonance in Medicine* 78:2373-2387, (2017).

[4] Ye C et al. Estimation of intravoxel incoherent motion parameters using low b-values. *PLoS One* 14:1-16, (2019).

[5] Jalnefjord O et al. Comparison of methods for estimation of intravoxel incoherent motion (IVIM) diffusion coefficient (D) and perfusion fraction (f). *Magnetic Resonance Materials in Physics, Biology and Medicine* 31:715-723, (2018).

[6] Orton MR, Collins DJ, Koh DM, Leach MO. Improved intravoxel incoherent motion analysis of diffusion weighted imaging by data driven Bayesian modeling. *Magnetic Resonance in Medicine* 71:411-420, (2014).

[7] Vidic I et al. Accuracy of breast cancer lesion classification using intravoxel incoherent motion diffusion-weighted imaging is improved by the inclusion of global or local prior knowledge with Bayesian methods. *Journal of Magnetic Resonance Imaging* 50:1478-1488, (2019).

[8] Le Bihan D, Breton E, Lallemand D, Grenier P, Cabanis E, Laval-Jeantet M. MR imaging of intravoxel incoherent motions: application to diffusion and perfusion in neurologic disorders. *Radiology* 161:401-407, (1986).

[9] Le Bihan D, Turner R, Moonen CT, Pekar J. Imaging of diffusion and microcirculation with gradient sensitization: design, strategy, and significance. *J Magn Reson Imaging* 1:7-28, (1991).

[10] Pekar J, Moonen CT, van Zijl PC. On the precision of diffusion/perfusion imaging by gradient sensitization. *Magn Reson Med* 23:122-129, (1992).

[11] Ginat DT et al. Diffusion-Weighted imaging for differentiating benign from malignant skull lesions and correlation with cell density. *American Journal of Roentgenology* 198: 597-601 (2012).

[12] Edrei Y et al. Improved efficacy of novel anti-angiogenic drug combination (TL-118) against colorectal-cancer liver metastases; MRI monitoring in mice. *British Journal of Cancer* 107: 658-666 (2012).